ARTICLE

Structural Dynamics of Phenyl Azide in Light-Absorbing Excited States: Resonance Raman and Quantum Mechanical Calculation Study[†]

Rong-dan Yuan, Jia-dan Xue, Xu-ming Zheng*

Department of Chemistry, Zhejiang Sci-Tech University, Hangzhou 310018, China

(Dated: Received on October 15, 2015; Accepted on December 8, 2015)

The excited state structural dynamics of phenyl azide (PhN_3) after excitation to the light absorbing $S_2(A')$, $S_3(A')$, and $S_6(A')$ states were studied using the resonance Raman spectroscopy and complete active space self-consistent field calculations. The vibrational spectra and the UV absorption bands were assigned on the basis of the Fourier transform (FT)-Raman, FT-infrared measurements, the density-functional theory computations and the normal mode analysis. The A-, B-, and C-bands resonance Raman spectra in cyclohexane, acetonitrile, and methanol solvents were, respectively, obtained at 273.9, 252.7, 245.9, 228.7, 223.1, and 208.8 nm excitation wavelengths to probe the corresponding structural dynamics of PhN_3. The results indicated that the structural dynamics in the $S_2(A')$, $S_3(A')$, and $S_6(A')$ states were significantly different. The crossing points of the potential energy surfaces, $S_2S_1(1)$ and $S_2S_1(2)$, were predicted to play a key role in the low-lying excited state decay dynamics, in accordance with Kasha's rule, and N7=N8 dissociation. Two decay channels initiated from the Franck-Condon region of the $S_2(A')$ state were predicted: the radiative $S_{2,min}\rightarrow S_0$ radiative decay and the $S_2\rightarrow S_1$ internal conversion through the crossing points $S_2S_1(1)/S_2S_1(2)$.

Key words: Phenyl azide, Structural dynamics, Decay dynamics, Resonance Raman spectroscopy, CASSCF calculation, Curve-crossing

I. INTRODUCTION

Photolysis of the aromatic azides (PhN_3) in UV light region has been known to produce the short-lived singlet phenylnitrene (PhN) intermediates and N_2 molecule [1–4]. The quantum yields were determined to be close to unity and in the range of 0.1−0.7 for the photodissociation of naphthyl azides and simple phenyl azides respectively [5–7]. The quantum chemical calculation revealed that the S_2 state of the azide was bound and there was a lower barrier toward arylnitrene formation in the S_1 state of the azide [7]. This consisted with the experimental observations that simple phenyl, biphenylyl, and naphthyl azides did not have any observable fluorescence. The early events of the photochemistry of three aryl azides (*para*- and *ortho*-biphenylyl azides, 1-naphthyl azide) were studied by ultrafast spectroscopy and quantum chemical calculations [8]. The S_2 state lifetimes of aryl azides were measured to be hundreds of femtoseconds by using the transient absorption spectroscopy. The S_2 state of the azides decayed with the growth of the transient absorptions of the corresponding singlet nitrenes. Quantum chemical calculations predicted that the arylnitrenes were formed in the S_1 states of the azides with a lower reaction barrier if the azides were initially populated in the S_2 state, in accordance with Kasha's rule [8]. The photochemistry of 4-amino-3-nitrophenyl azide, a widely used photoaffinity labeling system, was studied by using the transient absorption spectroscopy (femtosecond to microsecond time scale) and employing a theoretical perspective. The results showed that nitrene generated from the S_2 surface of azide, in violation of Kasha's rule [9].

Relative to the comprehensive studies of the nitrene chemistry, studies on the non-adiabatic decay dynamics and decomposition mechanism of aryl azides initiated from the light absorbing S_2 states were limited. It was not certain whether the singlet nitrene intermediate was formed from the light absorbing S_n ($n\geq 2$) states (in violation of Kasha's rule) or in the subsequent dark S_1 state (in accordance with Kasha's rule). Little has been known about the relationship between the quantum yields of the photodecomposition of the naphthyl azides and the decay channels of the formation of the corresponding niterenes. Therefore, in this work, the decay dynamics of phenyl azide initiated from the light absorbing S_2 state was studied by using the resonance Raman spectroscopy and quantum mechanical calculations. The resonance Raman spectra covering different

[†]Part of the special issue for "the Chinese Chemical Society's 14th National Chemical Dynamics Symposium".

*Author to whom correspondence should be addressed. E-mail: zxm@zstu.edu.cn, Tel.: +86-571-86843699

 ©2016 Chinese Physical Society

excited states were obtained to predict the underlying structural dynamics and the possible curve-crossings. CASSCF and TD-DFT calculations were carried out to reveal the excited state structures and help to determine the decay mechanism buried behind the resonance Raman intensity patterns. Both the radiative and non-radiative decay channels were found to occur in the S_2 state of the phenyl azide. The reaction mechanism of the nitrene formation were proposed.

II. EXPERIMENTS AND CALCULATIONS

The Fourier transform (FT)-Raman and FT-IR spectra were obtained with 2 cm^{-1} resolution using FT-Raman spectrometer at 1064 nm excitation (Thermo Nicolet 960, Thermo Fisher Nicolet, USA) and FT-IR spectrometer (Thermo Nicolet avatar 370, Thermo Fisher Nicolet, USA). The UV absorption spectra were measured using UV/visible spectrometer (UV-2501PC, Shimadzu, Japan).

The resonance Raman experimental method and apparatus have been described previously [10], so only a short description will be provided here. The harmonics of a nanosecond Nd:YAG laser and their hydrogen Raman shifted laser lines were employed to generate the 266.0, 273.9, 282.4, 299.1 and 309.1 nm excitation wavelengths utilized in the resonance Raman experiments. The excitation laser beam used a ∼100 μJ pulse energy loosely focused to a 0.5−1.0 mm diameter spot size onto a flowing liquid stream of sample. A backscattering geometry was employed for collection of the Raman scattered light by reflective optics that imaged the light through a polarizer and entrance slit of a 0.5 m spectrograph and the grating of the spectrograph dispersed the light onto a liquid nitrogen cooled CCD mounted on the exit of the spectrograph. The Raman shifts of the resonance Raman spectra were calibrated with the known vibrational frequencies of acetonitrile Raman bands. To fully subtract the solvent Raman bands from the resonance Raman spectra of the sample solutions and to accurately measure the absolute resonance Raman cross-sections, the sensitivity-correction [11–15] for the wavelength dependence of the efficiency of the collecting system (including the optical, the monochromator, and the detector), and the reabsorption-correction for the sample's absorbance in backscattering geometry [11, 12, 16] are taken into consideration, which uses our self-programming routine coded in Origin 6.0 software. The pure solvent Raman spectrum at certain excitation wavelength is scaled by a proper factor, which depends on the self absorption correction factor using angles of incidence which varies from 60° to 40° in our procedure, until the intensities of the scaled solvent Raman bands matches those of the corresponding bands in the sample resonance Raman spectrum at the same excitation wavelength. Sections of the resonance Raman spectra were fit to a baseline plus a sum of Lorentzian bands

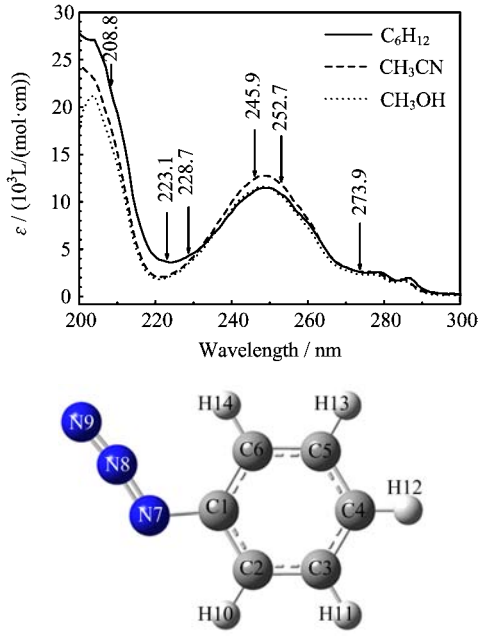

FIG. 1 The schematic diagram of the geometry structure and UV absorption spectra of PhN_3 in cyclohexane, acetonitrile and methanol.

to determine the integrated areas of the Raman bands of interest. The spectral resolution is about 3 cm^{-1} for the resonance Raman spectra.

The geometric structure optimization and vibrational frequency computation were done using the B3LYP/6-31+G(d) level of theory. The $S_0 \rightarrow S_n$ vertical transition energies were estimated at B3LYP-TD/6-31+G(d) levels of theory employing a self-consistent reaction field (SCRF), polarized continuum overlapping spheres model (PCM). The complete active space self-consistent field (CASSCF) theory was used to study the excited state structures and decay mechanism of PhN_3. The curve-crossing points between electronic excited states were computed at CASSCF(8,7)/6-31G(d) level. An active space with 8 electrons in 7 orbitals is referred to as CASSCF(8,7) hereafter. All of the quantum mechanical calculations were done using the Gaussian 03 program [17]. The normal mode analysis is done using the VEDA4 program coded by Jamróz [18].

III. RESULTS AND DISCUSSION

A. UV absorption spectra and electronic transitions

Figure 1 shows the schematic diagram of the geometry structure and the UV absorption spectra of PhN_3 in cyclohexane, acetonitrile and methanol with the laser excitation wavelengths indicated above the spectral curves. The experimental UV spectra in three solvents are in shape and in λ_{max} (wavelength at the

DOI:10.1063/1674-0068/29/cjcp1510213 ©2016 Chinese Physical Society

TABLE I B3LYP-TD/6-31+G(d) computed electronic transition energies and oscillator strengths f of PhN_3 in acetonitrile using PCM solvent model.

State	Orbital transition[a]	E_T/nm(eV)		f	
		Calculation	Experiment	Calculation	Experiment
$S_1(A'')$	$\pi_H \rightarrow \pi^*_L(0.69)+\pi_{H-2} \rightarrow \pi^*_L(0.14)$	295(4.20)		0.0006	
$S_2(A')$	$\pi_H \rightarrow \pi^*_{L+2}(0.52)+\pi_H \rightarrow \pi^*_{L+1}(0.34)+\pi_{H-1} \rightarrow \pi^*_{L+1}(0.31)+\pi_{H-1} \rightarrow \pi^*_{L+2}(-0.10)$	256(4.85)	279(A-band)	0.0352	0.0298
$S_3(A')$	$\pi_H \rightarrow \pi^*_{L+1}(0.58)+\pi_H \rightarrow \pi^*_{L+2}(-0.30)+\pi_{H-1} \rightarrow \pi^*_{L+1}(-0.18)+n_{H-3} \rightarrow \pi^*_L(-0.15)$	245(5.07)	248(B-band)	0.3184	0.2985
$S_4(A'')$	$\pi_{H-1} \rightarrow \pi^*_L(0.71)$	226(5.49)		0.0002	
$S_5(A')$	$\pi_H \rightarrow Ryd_1(0.69)+\pi_H \rightarrow Ryd_2(0.11)$	216(5.75)		0.0000	
$S_6(A')$	$\pi_{H-1} \rightarrow \pi^*_{L+1}(0.57)+\pi_H \rightarrow \pi^*_{L+2}(-0.35)+\pi_{H-2} \rightarrow \pi^*_{L+2}(-0.17)+\pi_{H-1} \rightarrow \pi^*_{L+2}(-0.12)$	208(5.97)	∼200(C-band)	0.2491	0.4995

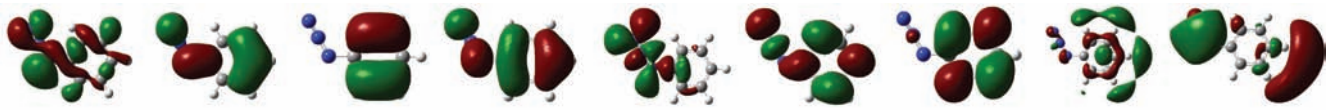

28: n_{H-3} 29: π_{H-2} 30: π_{H-1} 31: π_H 32: π^*_L 33: π^*_{L+1} 34: π^*_{L+2} 35: Ryd_1 36: Ryd_2

[a] The data in parentheses are orbital coefficents.

maximum absorption) very close to one another, and this suggests that the vertical electronic transition energies of PhN_3 depend little on the polarity and/or hydrogen bonding of solvents. Two broad experimental absorption bands are observed at λ_{max}=279 nm (A-band) and 248 nm (B-band) in acetonitrile respectively in 220−300 nm spectral region with the oscillator strength for B-band absorption (f=0.2985) being much larger than that for the A-band absorption (f=0.0298). Table I lists the B3LYP-TD/6-31G(d) computed electronic transition energies, the molecular orbitals, and oscillator strengths of PhN_3 in acetonitrile using PCM solvent model. The calculated results display two transition-allowed absorption bands at 245 nm (f=0.3184) and 256 nm (f=0.0352), and this correlates well with the B-band (248 nm) and A-band (279 nm) absorptions respectively.

According to Table I, the orbitals 31 and 29 are the highest and third highest occupied π bonding orbitals (referred as π_H and π_{H-2}) respectively with the corresponding electronic densities distributed among the whole molecular frame, while the orbital 30 is the second highest occupied π bonding orbital (π_{H-1}) with the electronic density mostly partitioned in the benzene moiety. The orbital 33 is the second lowest unoccupied π^* anti-bonding orbital (π^*_{L+1}) with the electronic density distributed among the whole molecular frame, while the orbital 34 is a π^*_{L+2} orbital with the electronic density partitioned mostly in the benzene moiety. The orbital 32 is the lowest unoccupied π^* anti-bonding orbital (π^*_L) formed via a Py-Py conjugation interaction of the N=N=N chromophore. Orbitals 35 and 36 are two diffuse orbitals, and they are designated as Ryd_1 and Ryd_2. Therefore the A-, and B-band absorptions are assigned as a combined $\pi_H \rightarrow \pi^*_{L+2}(0.52)+\pi_H \rightarrow \pi^*_{L+1}(0.34)+\pi_{H-1} \rightarrow \pi^*_{L+1}(0.31)+\pi_{H-1} \rightarrow \pi^*_{L+2}(-0.10)$ transitions and a combined $\pi_H \rightarrow \pi^*_{L+1}(0.58)+\pi_H \rightarrow \pi^*_{L+2}(-0.30)+\pi_{H-1} \rightarrow \pi^*_{L+1}(-0.18)+n_{H-3} \rightarrow \pi^*_L(-0.15)$ transitions.

B. Vibrational assignments of resonance Raman spectra

No report has been found on the vibrational assignments of PhN_3. We have carried out the vibrational assignments for PhN_3 with the aids of the density functional theory calculations, the normal mode analysis and the vibrational spectroscopic measurements in order to help to assign the resonance Raman spectra. Figure 2 shows the experimental FT-Raman and FT-IR spectra of PhN_3 in neat liquid and their correlation to the B3LYP/6-31+G(d) computed Raman spectrum. The normal mode analysis is also done to help the assignments. Table II lists the experimental and B3LYP/6-31+G(d) calculated vibrational frequencies as well as the vibrational assignments of PhN_3. The calculated vibrational frequencies are spectroscopically scaled through the linear-regression of the B3LYP/6-31+G(d) calculated frequencies to the experimental observed ones. It appears that the correlation between the experimental frequencies and the spectroscopically scaled calculated ones are in good agreement.

Figure 3 displays overall views of the resonance Raman spectra of PhN_3 in acetonitrile, methanol and cyclohexane at six excitation wavelengths that cover

DOI:10.1063/1674-0068/29/cjcp1510213 ©2016 Chinese Physical Society

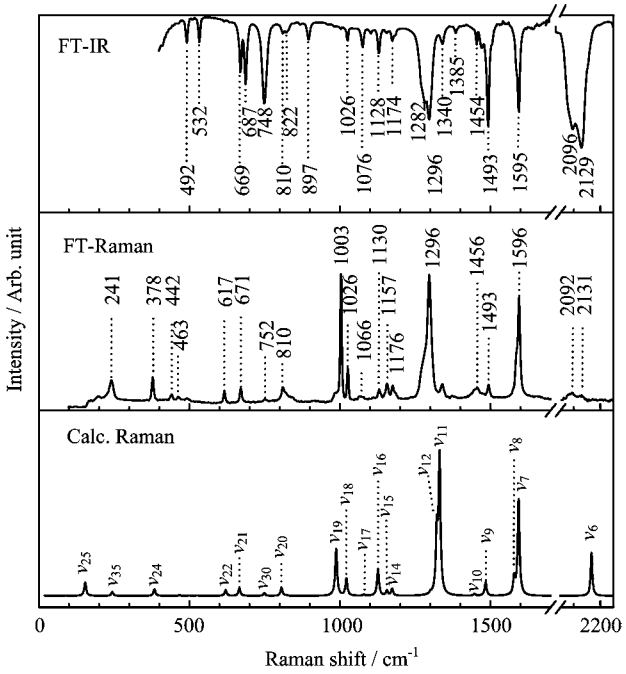

FIG. 2 Comparison of the FT-Raman and FT-IR spectra with the B3LYP/6-31+G(d) computed Raman spectrum of phenyl azide with the frequency value indicated.

across the A-, B-, and C-band absorptions. It shows that the intensity pattern of the resonance Raman spectra at a certain excitation wavelength in three different solvents is very similar to one another. This suggests that the polarity and/or the hydrogen bond of solvents have minor effect on the slope of the interested excited state potential energy surfaces in the Franck-Condon region. Keep in mind that the experimental oscillator strength measured for the B- band absorption is about 10 times that for the A-band, and that the Raman intensity is proportion to the square of the oscillator strength (f^2), we expect that 245.9 and 252.7 nm resonance Raman spectra shall mostly be in resonance with the $S_3(A')$ state (B-band), while 208.8 nm resonance Raman spectrum shall be in resonance with the $S_6(A')$ state (C-band).

Figure 4 shows the enlarged view of the resonance Raman spectra of PhN_3 in methanol. Most of the C-band resonance Raman spectra can be assigned as the fundamental modes ν_7, ν_{11}, ν_{19}, ν_9, and the overtones $2\nu_7$, $2\nu_{11}$, and combination bands $\nu_{11}+\nu_{19}$, $2\nu_{11}+\nu_{19}$, *etc.*, while most of the B-band resonance Raman spectra can be assigned as the fundamental modes ν_7, ν_{11}, ν_{19}, ν_9, ν_{14}, ν_{16}, ν_{20}, ν_{21}, ν_{22}, ν_{23}, ν_{24}, and the overtones $2\nu_{11}$, $3\nu_{11}$, $2\nu_7$, $3\nu_{14}$, and combination bands $\nu_{11}+\nu_{24}$, $\nu_{11}+\nu_{23}$, $\nu_{11}+\nu_{19}$, $\nu_{11}+\nu_{16}$, $\nu_{11}+\nu_{14}$, $2\nu_{11}+\nu_{19}$, $\nu_7+\nu_{24}$, $\nu_9+\nu_{14}$, $\nu_6+\nu_{11}$, $\nu_6+\nu_7$, *etc.* The intensity patterns for the C-, and B-band resonance Raman spectra are significantly different since the relative band intensities vary significantly for the most intense fundamental modes (ν_7, ν_{11}, ν_{19}, ν_9), their overtones and combination bands as the excitations wavelengths go from 252.4 nm to 208.8 nm. This suggests that the normal mode displacements of the four most intense modes (ν_7, ν_{11}, ν_{19}, ν_9) that are along the $S_3(A')$ excited state potential energy surfaces in the Franck-Condon region are considerably different from those that are along the $S_6(A')$ excited state potential energy surfaces. Owing to the very intense fluorescence interference, the 282.4 and 299.1 nm resonance Raman spectra are not obtained successfully. This retards us to extract the A-band short-time structural dynamics quantitatively.

The major difference in the intensity patterns between the 228.7 nm (or 223.1 nm) resonance Raman spectra and the B-band, or C-band resonance Raman spectra is that the former has a moderate N9N8/N8N7 stretch mode ν_6 at 2086 cm^{-1}, which is absent in the latter two spectra. Since the 228.7 and 223.1 nm excitation wavelengths fall in energy into the overlap region between the $S_3(A')$ and $S_6(A')$ states so that the corresponding resonance Raman spectra may contain important information on the state-coupling or curve-crossing among the higher-lying excited state. However, owing to the difficulties in the prediction of these curve-crossing points, we are unable to clarify the decay dynamics initiated from the $S_3(A')$ and $S_6(A')$ states.

Similarly, most of the 273.9 resonance Raman spectra can be assigned as approximately the thirteen fundamental modes (ν_7, ν_{11}, ν_{19}, ν_{10}, ν_9, ν_{14}, ν_{16}, ν_{20}, ν_{21}, ν_{22}, ν_{23}, ν_{24}, and ν_6), the overtones ($2\nu_{11}$ and $2\nu_7$), and the combination bands ($\nu_{11}+\nu_{24}$, $\nu_{11}+\nu_{22}$, $\nu_{11}+\nu_{19}$, $\nu_{11}+\nu_{16}$, $\nu_{11}+\nu_{14}$, $\nu_7+\nu_{24}$, $\nu_7+\nu_{22}$, $\nu_9+\nu_{14}$, $\nu_6+\nu_{11}$, *etc.*). The intensity patterns for the 273.9 and 252.4 nm resonance Raman spectra are similar. We expect that the intensities of the four most intense modes (ν_7, ν_{11}, ν_{19}, ν_{14}) in the 273.9 nm resonance Raman spectrum come from the B-band absorption since the oscillator strength (f=0.2985) of the B-band absorption is 10 times that of the A-band absorption and since the resonance Raman intensities are proportion to f^2. However, the major difference between the 273.9 and 252.7 nm resonance Raman spectra are noted owing to the significant resonance enhancement of the ν_{20}, ν_{21} and ν_{22} modes in the 273.9 nm spectrum. Since the 273.9 nm excitation wavelength falls in energy into the overlap region between the $S_2(A')$ and $S_1(A'')$ states, we expect that the corresponding resonance Raman spectra may contain important information on the state-coupling or curve-crossing among the higher-lying excited state.

C. Excited state structures and reaction dynamics

To explore the curve-crossings in the excited state decay processes and to understand the Franck-Condon region structural dynamics burried beneath the A-band resonance Raman intensity pattern, we have carried out

DOI:10.1063/1674-0068/29/cjcp1510213 ©2016 Chinese Physical Society

TABLE II B3LYP/6-31+G(d) computed and experimentally observed vibrational frequencies.

		Computed/cm^{-1}		Experiment/cm^{-1}			PED/%
		Calc.[a]	Scale[b]	FT-Raman	FT-IR	RR[c]	
A′	ν_1	3218(7/266)	3092				$\nu_{C2H}(57)+\nu_{C3H}(23)+\nu_{C4H}(15)$
	ν_2	3211(19/88)	3085				$\nu_{C4H}(39)+\nu_{C2H}(30)+\nu_{C5H}(24)$
	ν_3	3201(15/71)	3076				$\nu_{C6H}(35)+\nu_{C5H}(28)+\nu_{C3H}(18)+\nu_{C4H}(13)$
	ν_4	3193(3/105)	3068				$\nu_{C3H}(48)+\nu_{C6H}(28)+\nu_{C4H}(15)$
	ν_5	3185(3/22)	3061				$\nu_{C5H}(40)+\nu_{C6H}(31)+\nu_{C4H}(18)+\nu_{C3H}(10)$
	ν_6	2249(823/62)	2167	2092(vw)	2129(vs)	2083	$\nu_{N9N8}(80)+\nu_{N8N7}(20)$
	ν_7	1648(57/120)	1593	1595(s)	1595(s)	1587	$\nu_{C6C5(27)+}\nu_{C2C3}(15)+\nu_{C1C2}(15)+\nu_{C4C5}(10)$
	ν_8	1633(6/21)	1579	1587(m)	1587(m)		$\nu_{C3C4}(30)+\delta_{C1C2C3}(13)+\nu_{C1C2}(12)+\delta_{C6C5C4}(10)$
	ν_9	1534(79/17)	1484	1493(w)	1493(m)	1489	$\delta_{H14C6C5(20)+}\delta_{H11C3C2(19)+}\delta_{H13C5C4(14)+}\delta_{H10C2C1(13)}$
	ν_{10}	1495(1/2)	1447	1456(vw)	1454(vw)	1450	$\delta_{H12C4C3}(27)+\delta_{H13C5C4}(14)$
	ν_{11}	1373(98/161)	1330	1296(vs)	1296(s)	1287	$\nu_{N8N7}(21)+\nu_{C2C3}(12)+\delta_{H10C2C1}(12)+\nu_{N7C1}(10)$
	ν_{12}	1364(72/70)	1322	1280(m)	1282(s)		$\delta_{H14C6C5}(24)+\nu_{N8N7}(16)+\delta_{H10C2C1}(13)+\nu_{N7C1}(10)$
	ν_{13}	1342(19/2)	1301	1273(w)	1271(m)		$\nu_{C1C2}(27)+\delta_{H11C3C2}(12)+\nu_{C4C5}(12)+\nu_{C6C5}(10)$
	ν_{14}	1209(2/8)	1174	1176(vw)	1174(vw)	1168	$\delta_{H13C5C4}(27)+\delta_{H14C6C5}(18)+\delta_{H10C2C1}(13)+$ $\delta_{H11C3C2}(12)+\nu_{C6C5}(11)$
	ν_{15}	1190(0.1/5.7)	1156	1157(vw)			$\delta_{H12C4C3}(36)+\delta_{H11C3C2}(25)+\delta_{H13C5C4}(13)$
	ν_{16}	1160(17/30)	1127	1130(vw)	1128(w)	1123	$\delta_{C3C4C5}(23)+\delta_{C1C2C3}(15)+\nu_{N7C1}(13)+\nu_{N8N7}(7)$
	ν_{17}	1110(9/1.2)	1079	1066(vw)	1076(w)	1063	Ring deformation(89)
	ν_{18}	1050(4.5/19)	1022	1026(m)	1026(w)		$\nu_{C3C4}(24)+\nu_{C4C5}(21)+\delta_{H10C2C1}(10)$
	ν_{19}	1014(0.2/51)	988	1003(vs)	1003(vw)	998	$\delta_{C6C5C4}(32)+\delta_{C3C4C5}(21)+\delta_{C2C3C4}(16)$
	ν_{20}	824(5/8.6)	806	810(vw)	810(vw)	806	$\delta_{C3C4C5}(32)+\nu_{N7C1}(18)+\delta_{C2C3C4}(10)$
	ν_{21}	677(24/7.8)	666	671(w)	669(m)	664	$\delta_{N9N8N7}(33)+\delta_{N8N7C1}(29)+\delta_{C3C4C5}(14)$
	ν_{22}	629(0.2/5.9)	620	617(w)		603	$\delta_{C2C3C4}(40)+\delta_{C6C5C4}(23)+\delta_{C1C2C3}(11)$
	ν_{23}	469(0.4/0.8)	467	463(vw)		459	$\delta_{C1C2C3}(29)+\delta_{N9N8N7}(24)+\nu_{N7C1}(22)$
	ν_{24}	382(2.3/6.1)	384	378(m)		367	$\delta_{N7C1C6}(47)+\delta_{N9N8N7}(15)$
	ν_{25}	141(0.7/12)	154				$\delta_{N8N7C1}(51)+\delta_{N7C1C6}(22)+\delta_{N9N8N7}(21)$
A″	ν_{26}	997(0.1/0.4)	971	985(vw)			$\tau(93)$
	ν_{27}	975(0.1/0.01)	950				$\tau(85)$
	ν_{28}	911(5.3/0.05)	889		897(w)		$\rho_{tH12C4C5C6}(34)+\rho_{tH14C6C5C4}(27)+\rho_{tH10C2C1H6}(22)$
	ν_{29}	841(0.06/0.6)	822		822(w)		$\rho_{tH14C6C5C4}(33)+\rho_{tH10C2C1H6}(27)+\rho_{tH11C3C2C1}(22)+$ $\rho_{tH13C5C6C1}(15)$
	ν_{30}	764(71/2.7)	749	752(vw)	748(s)		$\rho_{tH12C4C5C6}(28)+\rho_{tH13C5C6C1}(26)+\rho_{tH11C3C2C1}(24)+$ $\gamma_{N7C1C2C6}(16)$
	ν_{31}	697(24/0.1)	685		687(m)		$\rho_{tC1C2C3C4}(37)+\gamma_{H12C}(15)+\gamma_{H13C}(13)+\rho_{tC6C5C4C3}(13)+$ $\gamma_{H10C}(12)$
	ν_{32}	531(10/0.4)	526		532(w)	520	$\rho_{tN9N8N7C1}(92)$
	ν_{33}	503(4.7/0.3)	500		492(w)	490	$\gamma_{N7C1C2C6}(54)+\rho_{tC2C3C4C5}(12)+\rho_{tC6C5C4C3}(11)+$ $\rho_{tH10C2C1C6}(10)$
	ν_{34}	420(0.0/0.04)	420				$\tau(89)$
	ν_{35}	235(0.00/3.5)	244	241(w)			$\tau(69)+\gamma_{N7C1C2H6}(23)$
	ν_{36}	74(0.04/0.3)	90				$\rho_t(89)$

Note: vs: very strong, s: strong, m: middle, w: weak, vw: very weak, sh:shoulder, ν: stretching, sym: symmetry, asym: asymmetry, δ: in-plane bending, γ: out-of-plane bending, ρ_t: twisting, τ: torsion, PED: potential energy distribution, only contributions larger than 10% were given.

[a] Values in parenthesis are IR/Raman activities.

[b] Scaled=19.42+0.955×calculated.

[c] Data from 245.9 nm resonance Raman spectrum in acetonitrile.

DOI:10.1063/1674-0068/29/cjcp1510213 ©2016 Chinese Physical Society

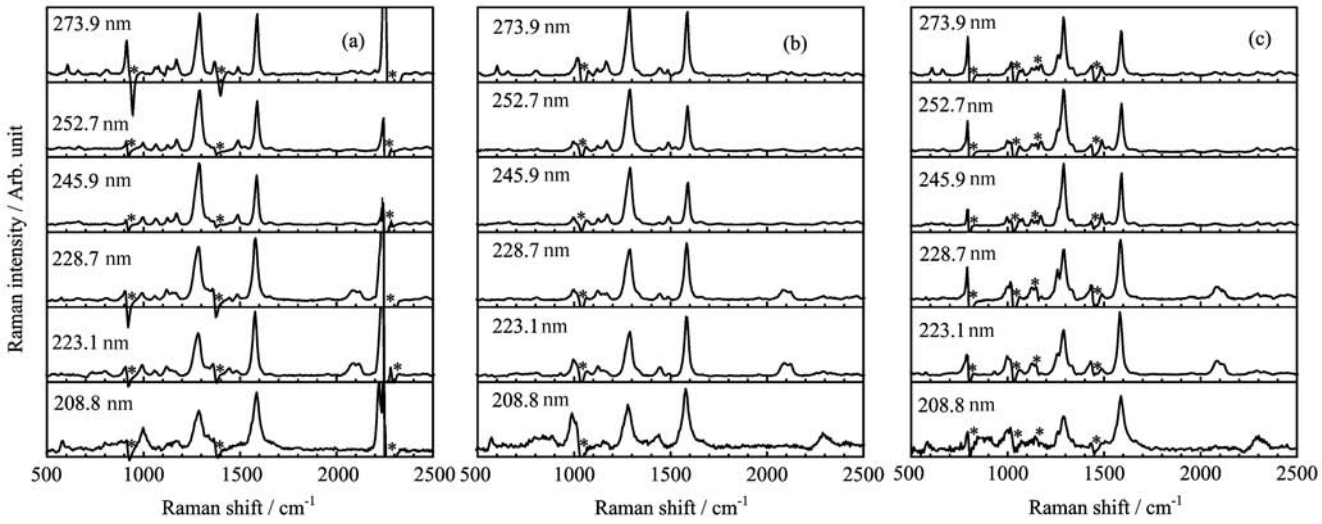

FIG. 3 Overview of the 273.9, 252.7, 245.9, 228.7, 223.1 and 208.8 nm resonance Raman spectra of phenyl azide in (a) acetonitrile, (b) methanol, and (c) cyclohexane. Asterisk (*) labels the solvent subtraction artifacts.

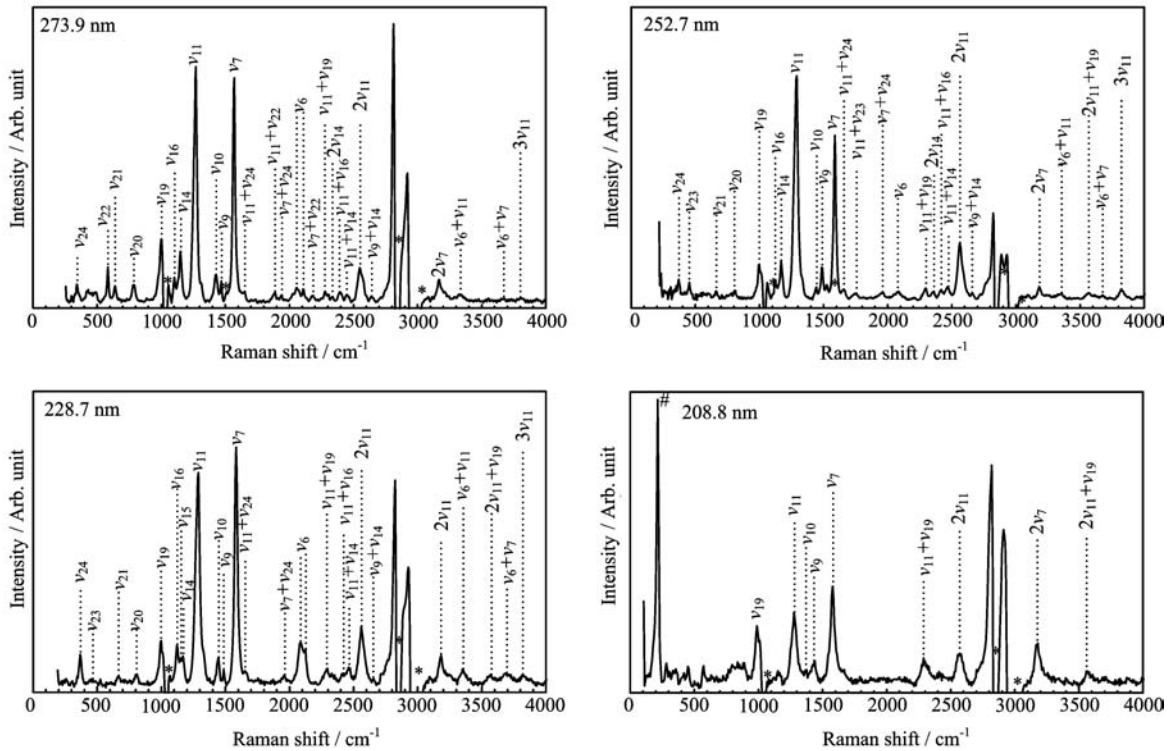

FIG. 4 Enlarged view of the 273.9, 252.7, 228.7, and 208.8 nm resonance Raman spectra of PhN_3 in methanol. Asterisk (*) labels the solvent subtraction artifacts. Pound ($^{\#}$) marks the residual uncertain laser line.

the CASSCF calculations. Table III lists the calculated vertical excitation energies and geometric structural parameters of the lower-lying singlet excited states and the corresponding curve-crossing points. Figure 5 displays the schematic diagram of the geometric structures for the above excited states and curve-crossing points.

The lowest light absorbing state is the $S_2(\pi\pi^*, A')$ state according to both CASSCF and TD-B3LYP calculations. It was previously known that simple phenyl, biphenylyl, and naphthyl azides did not have any observable fluorescence, which was explainable by their large quantum yields for extrusion of molecular nitro-

DOI:10.1063/1674-0068/29/cjcp1510213 ©2016 Chinese Physical Society

TABLE III Vertical excitation energy ΔE (in kcal/mol) and geometric structural parameters of the singlet excited states and conical intersection points with the bond length R in Å, the bond angle A in (°), and D of C−N=N=N in (°).

State	Sym.	Energy	ΔE	$R_{C1=C2}$	$R_{C2=C3}$	$R_{C1=C6}$	$R_{C5=C6}$	R_{C1-N7}	$R_{N7=N8}$	$R_{N8=N9}$	$A_{C-N=N}$	$A_{N=N=N}$	D
S_0	C_s	−393.4862396		1.406	1.379	1.375	1.402	1.412	1.246	1.119	115.6	173.3	180
$S_{1,FC}$		−393.3020627	116										
$S_{2,FC}$		−393.2198063	167										
$S_{3,FC}$		−393.2197987	167										
$S_{1,min}$	C_s	−393.3943425	57.7	1.415	1.377	1.381	1.399	1.387	1.380	1.170	112.4	118.0	180
$S_{2,min}$	C_1	−393.3072496	112	1.447	1.340	1.450	1.361	1.397	1.377	1.194	112.2	118.8	171.6
S_1S_0	C_s	−393.3778066	68.0	1.422	1.360	1.413	1.393	1.358	1.396	1.146	114.2	126.6	180
$S_2S_1(1)$	C_1	−393.3010573	116	1.452	1.428	1.455	1.433	1.279	1.389	1.190	116.0	128.6	105.5
$S_2S_1(2)$	C_1	−393.3468061	87.5	1.384	1.385	1.389	1.384	1.404	1.311	1.263	129.3	104.2	157.5
S_3S_2	C_s	−393.2928037	121	1.442	1.341	1.447	1.342	1.402	1.338	1.229	113.1	115.3	180

gen [7]. Herein, the existence of the $S_{2,min}$ structure is detected for the first time by the experimentally observed fluorescence spectra that accompany the 266.0, 273.9, and 282.4 nm resonance Raman scattering. This fluorescence spectrum (centered at λ_{max}=294 nm or 97 kcal/mol relative to S_0) red-shifts about 14 nm relative to the A-band absorption in cyclohexane, and is close to the transition energy (112 kcal/mol) of $S_{2,min}$ structure predicted by CASSCF calculation. The fluorescence at 294 nm is surely not originated from $S_{1,min}$→S_0 transition since it is estimated at ∼500 nm on the basis of our CASSCF calculations listed in Table III. The 294 nm concomitant fluorescence spectra observed in our resonance Raman experiments consists apparently with the ultrafast transient absorption spectroscopic observation that the S_2 state of azides that have lifetimes of hundreds of femtoseconds [8]. Therefore the 294 nm fluorescence spectrum of phenyl azide, assigned as the $S_{2,min}$→S_0 transition, serves as the efficient radiative decay channel of PhN_3 in the populated S_2 state. The structureless band shape of the $S_{2,min}$→S_0 fluorescence spectrum suggests that the band broadening is mostly due to the pure electronic dephasing or the very short lifetime of the S_2 state, but unlikely due to the solvent-induced inhomogeneous broadening.

The transition energies of the curve-crossing points $S_2S_1(1)$ and $S_2S_1(2)$ are determined to be 116 and 87.5 kcal/mol at CASSCF(8,7) level of theory. The transition energy of $S_2S_1(1)$ is higher than $S_{2,min}$ (112 kcal/mol) by 4 kcal/mol, while that of $S_2S_1(2)$ is higher than $S_{1,min}$(57.7 kcal/mol) by 30 kcal/mol. This suggests that when PhN_3 is initially populated in the S_2 potential energy surface, it can cross to the dark S_1 state through both $S_2S_1(1)$ and $S_2S_1(2)$, with $S_2S_1(1)$ being more close to the Franck-Condon region according to the geometry structures.

The lowest electronic state is the dark $S_1(\pi_H\pi^*_L, A'')$. As Table I shows, the lowest unoccupied anti-bonding π^*_L orbital is formed from the Py-Py conjugation interaction of the N=N=N chromophore. Thus one would expect that the -N7=N8=N9 chromophore undergoes large N7=N8 or N8=N9 bond length lengthening upon π_H→π^*_L(0.69) transition. As expected, CASSCF calculations reveal that the N7−N8 and N8−N9 bond lengths of the $S_{1,min}$ structure are 1.380 and 1.197 Å, longer than the corresponding 1.246 and 1.119 Å for S_0 by 0.134 and 0.078 Å respectively. This indicates that the N7−N8 and N8−N9 bonds become weakly bonded in S_1,min. Moreover, the transition energy for S_1,min is 57.7 kcal/mol, much lower than that for $S_2S_1(2)$. Thus upon internal-converting to the dark S_1 state, ∼30 kcal/mol available energy may make the initially populated S_1 state of PhN_3 highly vibrational excited so that the predicted N7−N8 bond dissociation may take place [7].

The Franck-Condon region structural dynamics of PhN_3 in the $S_2(A')$ and $S_3(A')$ state potential energy surfaces (A-, and B-band absorptions) is mostly along the vibration coordinates of ν_{11}, ν_7, ν_9, ν_{14}, ν_{19} on the basis of the resonance Raman spectra in Fig.3 and Fig.4. The most intense fundamental bands and overtone progressions appear in the N8N7(21%)+C2C3(12%)+N7C1(10%) stretch+H10C2C1(12%) in plane bend mode ν_{11}, the C6C5(27%)+C2C3(15%)+C1C2(15%)+C4C5(10%) stretch mode ν_7, $2\nu_{11}$ and $2\nu_7$. This suggests that the predominant structural dynamics occurs along ν_{11} and ν_7. The appearance of the intense ν_7 mode consists qualitatively with the major π_H→π^*_{L+2}(−0.32 or 0.52) electronic transition for the S_3 or S_2 state, which changes the C2−C3, C6−C5, C4−C5 and C1−C2 bond orders, while the appearance of the ν_{11} mode can partially be explained by the π_H→π^*_{L+1}(0.58 or 0.34) transition since it weakens N8N7 bond but enhances N7C1 and C2C3 bonds.

As mentioned above, the major difference between the A- and B-band resonance Raman spectra is that the A-band spectrum displays noticeable inten-

DOI:10.1063/1674-0068/29/cjcp1510213 ©2016 Chinese Physical Society

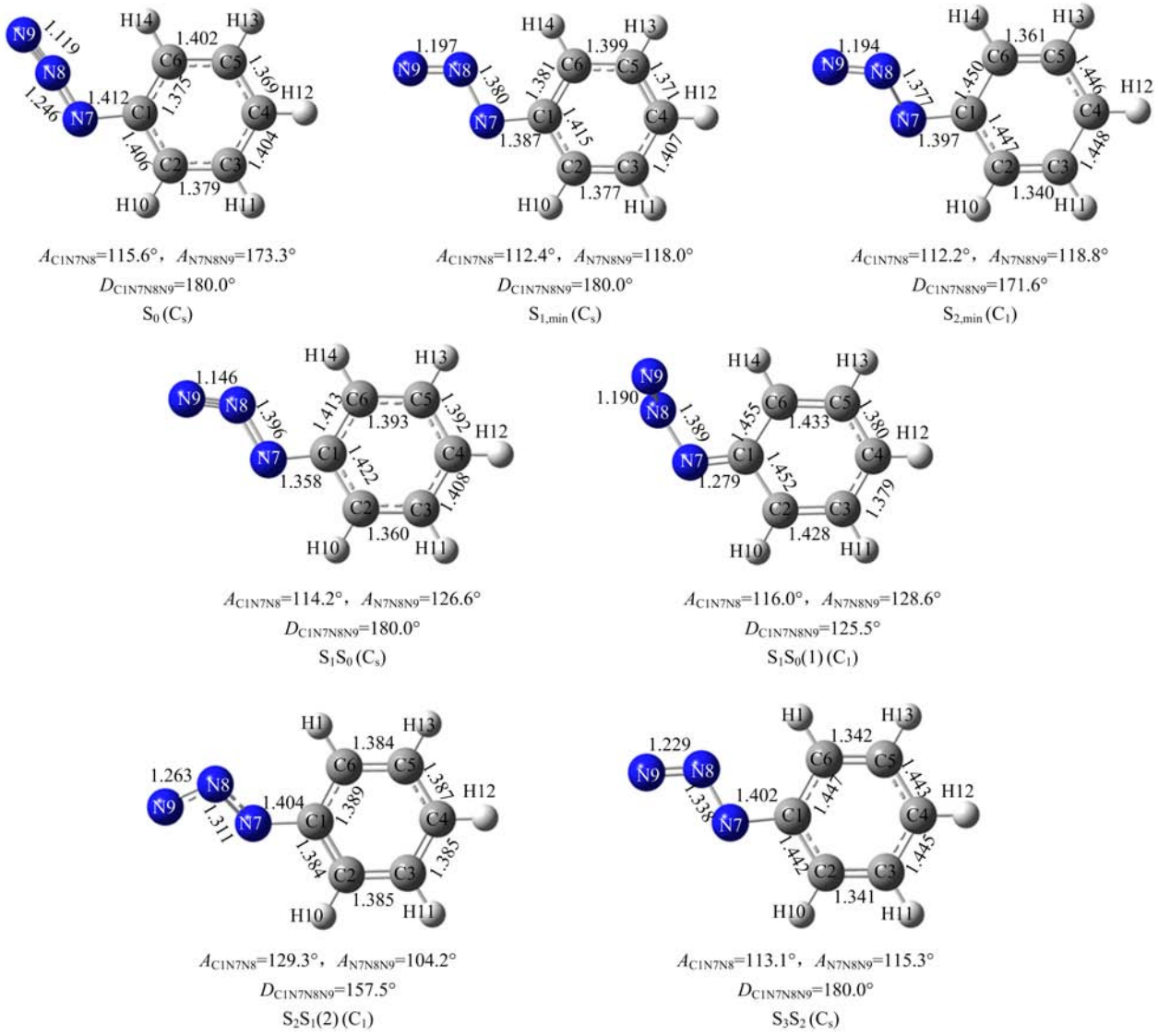

FIG. 5 Schematic diagram of the geometry structure of the lower-lying excited states and the corresponding curve-crossing points predicted at the CASSCF(8,7) level of theory.

sity increase in the fundamentals of the C3C4C5 in plane bend (32%)+N7C1(18%) stretch mode ν_{20}, the N9N8N7(33%)+N8N7C1(29%)+C3C4C5(14%) in plane bend mode ν_{21}, and the C2C3C4(40%)+C6C5C4(23%)+C1C2C3(11%) in plane bend mode ν_{22}. Their intensity enhancements are surely not due to the B-band absorption since they are much weaker in the 252.4 nm resonance Raman spectra. Thus these three Franck-Condon active modes are characteristic to the 273.9 nm resonance Raman spectrum. Keep in mind that the oscillator strength for the A-band absorption is only 10% that of the B-band absorption, we expect that PhN_3 undergoes substantial structural changes along the ν_{20}, ν_{21}, and ν_{22} vibrational reaction coordinates in the S_2 potential energy surface in the Franck-Condon region.

Quantitative correlation of the A-band short-time structural dynamics of PhN_3 to the CASSCF calculated S_2S_1 or $S_{2,min}$ structure requires both the well separated A-, and B-band absorptions and the quantitative simulation of the A-band resonance Raman spectra using time-dependent wave-packet so as to obtain the final short-time structural dynamics in terms of the easy-to-visualize internal coordinates. However the much intense B-band absorption retards our effort to extract at the quantitative or semi-quantitative level the A-band short-time dynamics in terms of the easy-to-visualize internal coordinates owing to the severe pre-resonance-resonance interference of the B-band absorption.

Qualitatively, the significant structural dynamics along the ν_{20}, ν_{21}, and ν_{22} vibrational coordinates suggests that the major part of the initial wave-packets

DOI:10.1063/1674-0068/29/cjcp1510213 ©2016 Chinese Physical Society

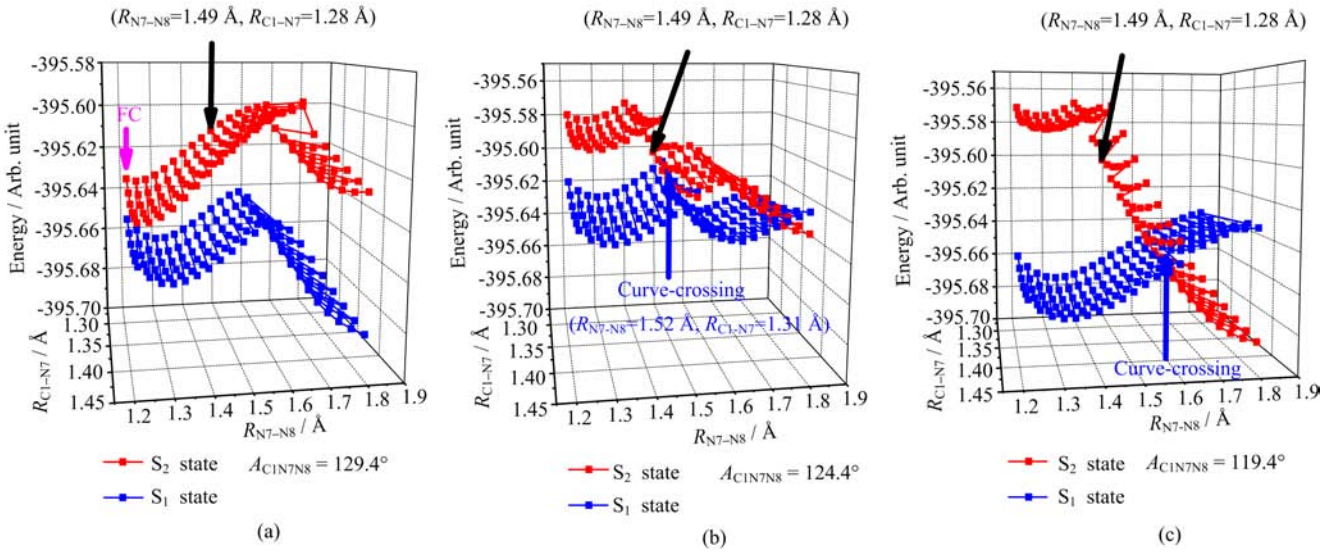

FIG. 6 3D rigid potential energy surface scans of the S_1 and S_2 states of PhN_3 with the R_{C1-N7} and R_{N7-N8} and the $A_{C1-N7-N8}$ being varied. At TD-B3LYP level of theory, the scan initiates at the Franck-Condon point of the ground state geometry (a), and then with the $A_{C1-N7-N8}$ being set to 124.4° (b) and 119.4° (c). In situation C, the S_2 potential energy becomes predissociative when the R_{N7-N8} is longer than about 1.45 Å. The black arrow serves as a reference point where the energy fluctuation for the S_2 potential surface is small at each scan. The blue arrow shows the curve-crossing point for each scan.

is along the $S_2(A')$ potential energy surface since no vibrational mode in A'' is noticeably observed in the 273.9 nm resonance spectrum, and this can correlate either to the S_2,min or S_2S_1 structure. As the first step towards understanding the roles of the ν_{20}, ν_{21}, and ν_{22} modes in the photodissociation dynamics of PhN_3 upon A-band absorption, we have carried out the 3D rigid potential energy surface scans for the S_1 and S_2 states using TD-B3LYP level of theory. For each scan, three variables are chosen among the internal coordinates of the R_{C1-N7}, R_{N7-N8}, and R_{N8-N9} bonds and the $A_{C1-N7-N8}$ and $A_{N7-N8-N9}$ bond angles. Figure 6 depicts the potential energy surfaces scans using variables of R_{C1-N7}, R_{N7-N8}, and $A_{C1-N7-N8}$. The result indicates that at $A_{C1-N7-N8}\approx124°$ the S_2 state internal-converts to the S_1 state, which is somewhat larger than $A_{C1-N7-N8}\approx129°$ for S_2S_1 predicted by the CASSCF(8,7) calculation. Further decrease of the C1−N7−N8 bond angle makes PhN_3 in the S_2 state become dissociative along the N7−N8 bond coordinate. The potential energy surfaces scans using variables of other combinations without including the C1−N7−N8 bond angle were also carried out, and the results indicates that there is no curve-crossing taking place at each scan. Apparently the C1−N7−N8 bond angle motion controls the curve-crossing between S_2 and S_1 state and the final nitrene formation through the N7−N8 bond dissociation of PhN_3.

Further examination of Fig.5 shows that the most important structural differences between $S_2S_1(2)$ and S_0 for the CN7N8N9 moiety are the significant changes of the $A_{C1-N7-N8}$ (129.3°) and $A_{N7-N8-N9}$ (104.2°) bond angles for S_2S_1 relative to those (115.6° and 173.3° respectively) for S_0, which is contrast to the minor change of the $A_{C1-N7-N8}$ (112.2°) for $S_{2,min}$ relative to that (115.6°) for S_0. Thus the appearance of the mode ν_{21} in the 273.9 nm resonance Raman spectrum but absent in the 252.4 nm resonance Raman spectrum suggests that the initial S_2 state structural dynamics revealed by the 273.9 nm resonance Raman spectrum is likely towards the $S_2S_1(2)$ structure but does not correlate to the $S_{2,min}$ structure, which indicates that the $S_2S_1(2)$ curve-crossing takes place somewhere not far away from the Franck-Condon region.

IV. CONCLUSION

In this work, the excited state structures and decay dynamics of phenyl azide (PhN_3) after excitation to the light absorbing $S_2(A')$, $S_3(A')$, and $S_6(A')$ states are determined according to the CASSCF calculations and the resonance Raman spectroscopic measurements. The vibrational FT-Raman and FT-IR spectra are assigned on the basis of experimental spectroscopic measurements, the DFT calculations, and the normal mode analysis. At CASSCF(8,7)/6-31G(d) level of theory, the low-lying excited state structures of $S_{1,min}$, $S_{2,min}$, S_1S_0, $S_2S_1(1)$, $S_2S_1(2)$, S_3S_2 are predicted. The 294 nm concomitant fluorescence observed in our resonance Raman experiments is assigned as the $S_{2,min}\rightarrow S_0$ transition. Two decay channels initiated from the FC

DOI:10.1063/1674-0068/29/cjcp1510213 ©2016 Chinese Physical Society

region of the S_2 state are determined. One is the $S_{2,FC}\rightarrow S_{2,min}\rightarrow S_0$ radiative decay channel that makes PhN_3 return directly to the ground state. The other is the $S_{2,FC}\rightarrow S_2S_1\rightarrow S_1$ nonradiative decay channel to form the dark S_1 state, where the further N7−N8 dissociation takes place to form phenyl nitrene and N_2.

V. ACKNOWLEDGMENTS

This work is supported by the National Natural Science Foundation of China (No.21473163, No.21033002, No.21202032) and the National Basic Research Program of China (No.2013CB834604).

[1] W. Lwowski Ed., *Nitrenes*, Wiley: New York, (1970).
[2] D. S. Breslow, *Azides and Nitrenes*, E. F. V. Scriven, ed., Orlando, FL: Academic Press, 491 (1984).
[3] H. Bayley, *Photogenerated Reagents in Biochemistry and Molecular Biology*, New York: Elsevier Press, (1983).
[4] S. A. Fleming, Tetrahedron, **51**, 12479 (1995).
[5] M. F. Budyka, N. V. Biktimirova, T. N. Gavrishova, and O. D. Russ. Laukhina, J. Phys. Chem. **79**, 1666 (2005).
[6] R. F. Jenkins, W. H. Waddell, and H. W. Richter, J. Am. Chem. Soc. **109**, 1583 (1987).
[7] M. W. Geiger, M. M. Elliot, V. D. Karacostas, T. J. Moricone, J. B. Salmon, V. L. Sideli, and M. A. St. Onge, Photochem. Photobiol. **40**, 545 (1984).
[8] G. Burdzinski, J. C. Hackett, J. Wang, T. L. Gustafson, C. M. Hadad, and M. S. Platz, J. Am. Chem. Soc. **128**, 13402 (2006)
[9] V. Voskresenska, R. M. Wilson, M. Panov, A. N. Tarnovsky, J. A. Krause, S. Vyas, A. H. Winter, and C. M. Hadad, J. Am. Chem. Soc. **131**, 11535 (2009)
[10] X. Zheng, Y. L. Li, and D. L. Phillips, J. Phys. Chem. A. **108**, 8032 (2004).
[11] A. B. Myers, *in Laser Techniques in Chemistry*, A. B. Myers and T. R. Rizzo Eds., New York: Wiley, 325 (1995).
[12] A. B. Myers and R. A. Mathies, *in Biological Applications of Raman Spectroscopy*, T. G. Spiro Ed., New York: Wiley, 2 (1987).
[13] R. Ouillon and S. Adam, J. Raman Spectrosc. **12**, 281 (1982).
[14] F. J. Purcell, R. Kaminski, and E. Russavage, Appl. Spectrosc. **34**, 323 (1980).
[15] J. R. Scherer and S. Kint, Appl. Optics. **9**, 1615 (1970).
[16] A. B. Myers, B. Li, and X. Ci, J. Chem. Phys. **89**, 1876 (1988).
[17] M. J. Frisch, G. W. Trucks, H. B. Schlegel, G. E. Scuseria, M. A. Robb, J. R. Cheeseman, J. A. Montgomery Jr., T. Vreven, K. N. Kudin, J. C. Burant, J. M. Millam, S. S. Iyengar, J. Tomasi, V. Barone, B. Mennucci, M. Cossi, G. Scalmani, N. Rega, G. A. Petersson, H. Nakatsuji, M. Hada, M. Ehara, K. Toyota, R. Fukuda, J. Hasegawa, M. Ishida, T. Nakajima, Y. Honda, O. Kitao, H. Nakai, M. Klene, X. Li, J. E. Knox, H. P. Hratchian, J. B. Cross, C. Adamo, J. Jaramillo, R. Gomperts, R. E. Stratmann, O. Yazyev, A. J. Austin, R. Cammi, C. Pomelli, J. W. Ochterski, P. Y. Ayala, K. Morokuma, G. A. Voth, P. Salvador, J. J. Dannenberg, V. G. Zakrzewski, S. Dapprich, A. D. Daniels, M. C. Strain, Ö. Farkas, D. K. Malick, A. D. Rabuck, K. Raghavachari, J. B. Foresman, J. V. Ortiz, Q. Cui, A. G. Baboul, S. Clifford, J. Cioslowski, B. B. Stefanov, G. Lui, A. Liashenko, P. Piskorz, I. Komaromi, R. L. Martin, D. J. Fox, T. Keith, M. A. Al-Laham, C. Y. Peng, A. Nanayakkara, M. Challacombe, P. M. W. Gill, B. Johnson, W. Chen, M. W. Wong, C. Gonzalez, and J. A. Pople, *Gaussian 03, Revision B.02*, Pittsburgh, PA: Gaussian Inc., (2003).
[18] M. H. Jamróz, *Vibrational Energy Distribution Analysis: VEDA 4 Program*, Warsaw, (2004).

DOI:10.1063/1674-0068/29/cjcp1510213 ©2016 Chinese Physical Society